# Synaptic-like Conductivity and Plasticity in Epitaxially Strained $SrTiO_3$ Films

Y. Dai, J. Schubert, S. Trellenkamp, G. Mussler, and R. Wördenweber

*Institute of Complex Systems (ICS), Forschungszentrum Jülich, D-52425 Jülich, Germany*

*Contact:* r.woerdenweber@fz-juelich.de;

yang.dai@siat.ac.cn

**Abstract**

In this work we use epitaxial strain and an asymmetric electrode design to engineer the conductivity of $SrTiO_3$ thin films in order to use them as active components in planar artificial synaptic devices. First, the tensile strain imposed by the rare-earth scandate substrate on epitaxial grown $SrTiO_3$ films results in a significant increase of the conductivity of the $SrTiO_3$. Second, a further enhancement of the conductivity is obtained by the use of Ti/Pt electrodes. Finally, the asymmetric electrode design consisting of a flat and a tapered electrode ensures the asymmetric response and plasticity of electronic synapse. The modifications of the conductivity are explained in terms of changes in the density and mobility of oxygen vacancies. The resulting electronic synapses (e-synapse) show memristor behavior as well as the plasticity of the signal which both are essential characteristics of a synapse. Similar to the synaptic long-term and short-term potentiation/depression, our $SrTiO_3$ e-synapses show two different types of plasticity, a fast process associated with the ionic dipole formation (relaxation time in the 100 ps regime) and a slow process defined by the mobility of oxygen vacancies (relaxation time of several seconds).

**Keywords:**

tensile strain, oxygen vacancy, memristor, artificial synapsis

## I. Introduction

Motivated by the brain which is able to remember, learn, and process information in an energy-efficient and fault-tolerant way, the development of so-called neuromorphic systems – i.e. electronic systems that can mimic the function of the brain - is currently attracting a lot of significant interest [1-4]. Similar to the synapse in the brain, an artificial synapse is one of the most basic element in the neuromorphic system. It represents a special type of two-terminal memristor, namely an electronic synapse (e-synapse), which, additional to its ultra-low power consumption, involves two important properties: the classical switching and a new feature, the so-called plasticity. The latter allows the e-synapse to be modified by the switching itself, i.e. it is able to "learn" and "forget". There exist a number of electronic systems that exhibit a synapse-like behavior. They can be classified according to their mechanism into interface barrier based, filament based and other (e.g. spin or phase change) e-synapses. For instance, molecular and ionic thin-film memristive systems are based on the mobility of defects in the materials [5-8], insulator-to-metal phase transition driven memristors use the phase transition caused by the Joule heating [9], and ferroelectric memristors utilize the electronically driven polarization of the materials [10, 11]. One of the most pursued type of memristor is based on the uniform versus nonuniform oxygen diffusion in oxides [8]. In this type of materials, oxygen vacancies play the significant role in the resistive switching behavior. Different explanations for the diffusion of oxygen vacancy have been suggested ranging from the development of conductive filaments [12, 13], the modulation of the interface barrier height [14-16], and space-charge limited current effects [17]. The control of the oxygen vacancy diffusion in these materials represents one of the major issues of these promising type of memristor, especially in case of a "learning" e-synapse.

The perovskite represents an ideal candidate for the active element of an e-synapse since its conductivity can easily be modified by simply changing its defect concentration. In previous studies this has been achieved for instance by Cr-doping [18], varying the temperature or oxygen partial pressure during film growth [19], or thermal treatment at elevated temperatures [20]. Since the conductivity of $SrTiO_3$ is typically extremely small

even after the modification, in most cases vertical electrode-oxide-electrode arrangement consisting of sandwich structures with extremely thin films are used (see Fig. 1).

In this work, we use epitaxial strain to improve the density and mobility of oxygen vacancies and, thus, the electric transport properties of $SrTiO_3$ thin films. Our epitaxially grown $SrTiO_3$ thin films are tensily strained (typically ~1%) due to the lattice mismatch between film and the substrate. Without strain $SrTiO_3$ is a cubic perovskite and an insulator with a band gap of ~3.2 eV at room temperature. However, under strain the electronic conductance can be tuned (see Fig. 1):

(i) Lattice distortions modify the *band structure* of $SrTiO_3$ [21]. They affect the occupation of the oxygen 2*p* orbital, which then contributes to the density of states at the Fermi level and, thus, can enhance the conductivity for the direction of tensile strain [22].

(ii) Defects (most likely *oxygen vacancies*) are automatically generated in order to compensate the strain in strained film [23]. Moreover, in case of oxides the mobility of oxygen vacancies can be enhanced by the strain [24]. Whereas both effects are expected to lead to an enhanced conductivity in case of tensily strained $SrTiO_3$, the latter effect favors a plastic behavior of these films.

(iii) The *ferroelectric phase transition* $T_o$ of $SrTiO_3$ can be enhanced by tensile strain [25]. Since this phase transition is accompanied by a structural transition, it is expected that the mobility of the defects (oxygen vacancies) is enhanced at $T_o$. This offers a third option to modify the conductivity of $SrTiO_3$ via strain.

The resulting strain modification of the conductivity and plasticity is summarized in Fig. 1. In this paper we demonstrate that adequate tensile strain leads to (i) a larger conductivity (compared to unstrained $SrTiO_3$) which allows even lateral arrangements of the electrodes and makes this system quite flexible with respect to the design of devices, (ii) the desired large plasticity, and (iii) a high stability (robustness) of our e-synapses made from epitaxial thin-film $SrTiO_3$.

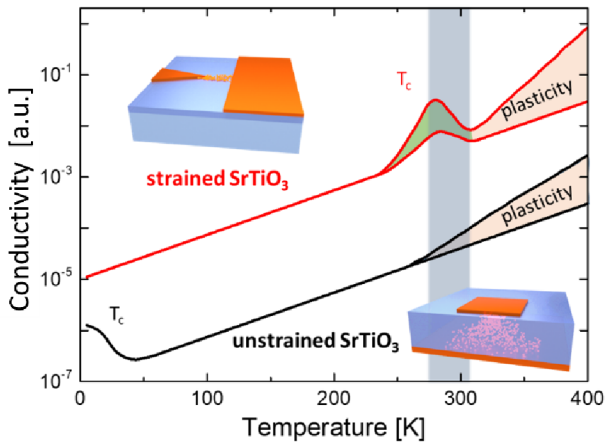


*Figure 1: Schematic of the impact of strain on the conductivity and plasticity of $SrTiO_3$ thin film e-synapse showing the general enhancement of the conductivity and the different temperature regimes of plasticity due to thermal activation at elevated temperature (orange) and at the ferroelectric phase transition (green). The different sketches show a typical vertical nanosize device used for unstrained $SrTiO_3$ memristors and the planar layout with electrodes on top of the $SrTiO_3$ layer used in this work.*

## II. Sample Preparation and Characterization

Epitaxial $SrTiO_3$ films with thicknesses ranging from 30 nm to 100 nm were deposited via pulsed laser deposition on (110) oriented $DyScO_3$, $TbScO_3$, and $GdScO_3$, substrates at a heater temperature of 850 °C in oxygen at 0.5 Pa, a laser power of 5 J/cm$^2$ (repetition rate 10 Hz) using stoichiometric single-crystalline $SrTiO_3$ targets, and a target-to-substrate-distance of approx. 55mm. The films grow epitaxially with a (001) orientation (see inserts of Fig. 2).

Due to the lattice mismatch between $SrTiO_3$ and the different rare-earth scandates, the in-plane lattice parameters ([100] and [010]) of $SrTiO_3$ are slightly elongated, whereas the [001] lattice parameter of $SrTiO_3$ is slightly reduced. Neglecting relaxation effects which typically set in for thicker films, the resulting strain in the epitaxial $SrTiO_3$ films on (101)$DyScO_3$ are 1.002%, 1.130%, and –0.637% for the different directions [100]$SrTiO_3$ (oriented along [$1\bar{1}0$] $DyScO_3$), [010]$SrTiO_3$ (oriented along [001]$DyScO_3$), and

[001]$SrTiO_3$ (oriented normal to the $DyScO_3$ surface), respectively. Slightly larger values are present for $SrTiO_3$ on the other rare-earth scandates $TbScO_3$ and $GdScO_3$. More details can be found in our previous work in ref. [23]. As a result, we obtain $SrTiO_3$ films with different in-plane tensile strain along a "short" ([100]) and "long" ([010]) axis. It has been shown, that the expansion of the in-plane lattice parameters strongly affects the phase transition temperature $T_o$ for the transition from the ferroelectric to paraelectric state [23]. The strain dependence of the closely related Curie temperature $T_C$ can be explained by the Landau thermodynamic theory:

$$T_C(\epsilon) = 2\varepsilon_0 C \frac{Q_{11} + Q_{12}}{s_{11} + s_{12}} \epsilon + T_C(0) \qquad (1)$$

where $\varepsilon_0$ is the permittivity of vacuum, $C$ is the Curie-Weiss constant, $Q_{ij}$ and $s_{ij}$ represent the electrostrictive coefficients and elastic compliances, and $\epsilon$ is the strain. Inserting reasonable values for $SrTiO_3$, i.e. $T_C(\varepsilon = 0)$ = 36 K, $C = 9\times10^4$ K [26], $Q_{11}+Q_{12}$ = -0.033 $m^4/C^2$ [27], and $s_{11} + s_{12} = 2.38 \times10^{-12}$ $m^2/N$ [28], we obtain a linear dependence of the phase transition temperature on the strain as shown in Fig. 2. It turns out that the films with a transition temperature slightly below room temperature (i.e. operating temperature of an e-synapse) are beneficial for the use in memristor devices (this is actually in agreement with the assumption sketched in Fig. 1 that a peak in the conductivity slightly below operation temperature might be beneficial for the performance of the e-synapse). In contrast to films deposited on $TbScO_3$ or $GdScO_3$, films on $DyScO_3$ operated more robust and show the required resistive switching behavior at room temperature. Therefore we will only report on the results obtained for the $SrTiO_3$ on $DyScO_3$ in the following.

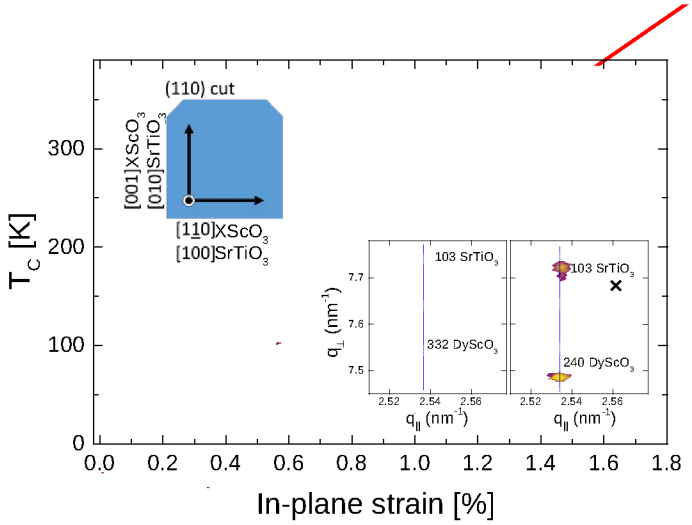


*Figure 2: Theoretical expectation (solid line, according to eq. (1)) and experimental data (symbols) of the strain dependence of the Curie temperature for $SrTiO_3$ and our $SrTiO_3$ films on various rare-earth scandates, respectively. The different symbols mark unstrained $SrTiO_3$ (solid circle) and the films grown on $DyScO_3$ (open triangles), $TbScO_3$ (solid triangles), and $GdScO_3$ (open diamonds). The inserts show the reciprocal space mapping of the XRD in the vicinity of the (332) (left) and the (240) (right) Bragg reflections of the substrates for a 90 nm thick $SrTiO_3$ film grown on (110)$DyScO_3$; the crosses indicate the positions of the corresponding XRD reflexes of unstrained $SrTiO_3$. The sketch indicates the crystallographic orientation of the $SrTiO_3$ in case of the growth on (110)$XScO_3$ (X=Dy, Tb, Gd).*

In order to study the electrical properties of the $SrTiO_3$ films, metal electrodes were deposited on top of the films using e-beam lithography and lift-off lithography technique [29]. Depending on the type of measurement different designs and metal combinations are chosen for the electrodes. The design for the resistive characterization of the film and the metal-oxide interface consists of two “flat” electrodes (extended plane-parallel electrodes, see for instance inserts of Fig. 3 and 4), whereas for the memristive devices a combination of a flat electrode and a sharply tapered electrode is used (see for instance insert of Fig. 5(a)). The electrodes consist either of a single Pt layer (thickness 50 nm) or a combination of a Ti layer (5 nm) and a Pt layer (50 nm).

## III. Results and Discussion

Before we get to the e-synapse, let us first discuss (i) the electronic behavior of the strained $SrTiO_3$ films and (ii) the role of the metal-oxide interface between the electrodes and the oxide film.

### A. Resistive behavior of strained $SrTiO_3$ films

Fig. 3 shows a comparison of the conductivity of two strained $SrTiO_3$ films of different thickness (deposited on (110)$DyScO_3$ and measured along the in-plane direction (here [010]$SrTiO_3$ direction)) and unstrained single crystalline $SrTiO_3$. In order to exclude the influence of the electrode-film interface (see section B below) [30] and record only the conductivity in the oxide film, a rather large gap of 3 µm between the electrodes has been chosen. This large gap size is compensated by a large electrode size (500 µm, see sketch in Fig. 3). Since the low-temperature data for the crystal fall below the resolution of this measurements (approx. $5 \cdot 10^{-8}$ S/m), the data of the single crystal are recorded in the nonlinear regime (here 3.3 V/µm). All other data are obtained in the ohmic regime, i.e. at low electric fields. Nevertheless the trends are clearly visible.

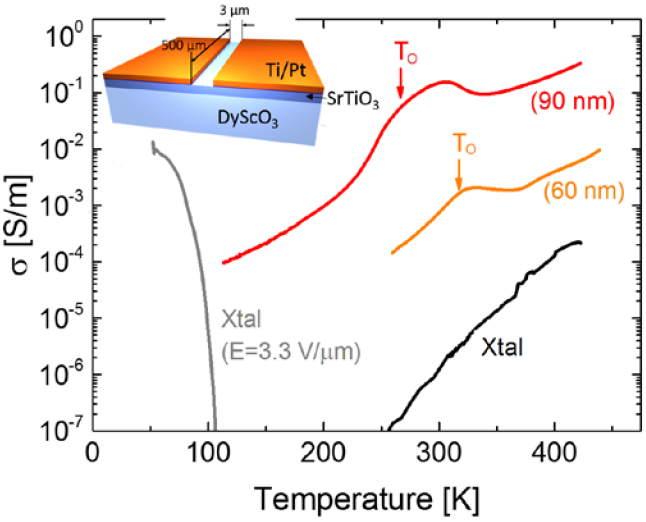


*Figure 3: Temperature dependence of the conductivity of a 90 nm and a 60 nm thick $SrTiO_3$ film on (110)$DyScO_3$ measured along the large strain ([010]$SrTiO_3$) direction and, for*

*comparison, of unstrained $SrTiO_3$ (single crystal). All measurements represent the conductivity at small electric fields, i.e. in the ohmic regime, except for the low temperature data for crystalline $SrTiO_3$ (gray line) which was measured at elevated field (3.3 V/µm) in order to obtain a measurable signal above the noise floor of ~ $5 \cdot 10^{-8}$ S/m. The phase transition temperature $T_o$ for strained $SrTiO_3$ is marked, the insert shows a sketch of the electrode design and the arrangement of the layers.*

Although especially the measurements of the conductivity of the strained films turn out to be difficult due to their "plasticity" (which represents the most important property of these films and will be discussed later), there are a number of interesting features visible in Fig. 3:

(i) Generally the conductivity is larger in the strained films compared to that of the unstrained single crystal. The enhanced conductivity might be a result of the enhanced density of defects (esp. oxygen vacancies) that are automatically generated by the strain in these films [23, 31].

(ii) In all cases a peak in the conductivity can be seen which seems to be associated with the ferroelectric phase transition [32, 33]. This peak is visible for the strained films. In analogy we observe a strong increase of the conductance of the unstrained $SrTiO_3$ at low temperature (indicating the approach of the 'non-existing' ferroelectric transition of the incipient ferroelectric material) if we extend the measurement to large electric fields (i.e. to the non-ohmic regime). Due to the strain-induced shift of $T_o$, this peak is shifted towards room temperature for our strained films on $DyScO_3$. This peak might be one reason for the robustness of these films in memristor devices (see also idealized sketch Fig. 1).

(iii) Finally, excluding the peak at $T_o$, generally the conductivity increases with increasing temperature in a more or less exponential way. This also defines an optimum for the operation of these films in memristor or e-synapse devices.

The increased conductivity of the strained films including the peak in the conductivity just below room temperature is one of the major reasons to choose $SrTiO_3$ on $DyScO_3$ for further memristor and neuromorphic experiments.

### B. Metal-oxide interface of strained $SrTiO_3$

It is known from literature, that the choice of metal can strongly affect the transport behavior of metal-oxide interface [30, 34, 35]. For instance, it is reported that Ti deposited on $TiO_2$ can create a high density of oxygen vacancies near a metal/semiconductor interface [14]. These oxygen vacancies can also be beneficial for the resistive behavior of oxide films [36-38]. Meanwhile, the height of the Schottky barrier in the metal-oxide interface can be decreased by substituting the electrode with a low work function metal. Therefore we tested two different types of metallic electrodes for our strained $SrTiO_3$ films, i.e. Pt-electrodes and a metallic bilayer consisting of Ti and Pt. In the first case the metal-oxide interface is formed by $SrTiO_3$/Pt, in the second case it is defined by $SrTiO_3$/Ti. The thickness of the Ti and Pt layers are always 5 nm and 50 nm, respectively.

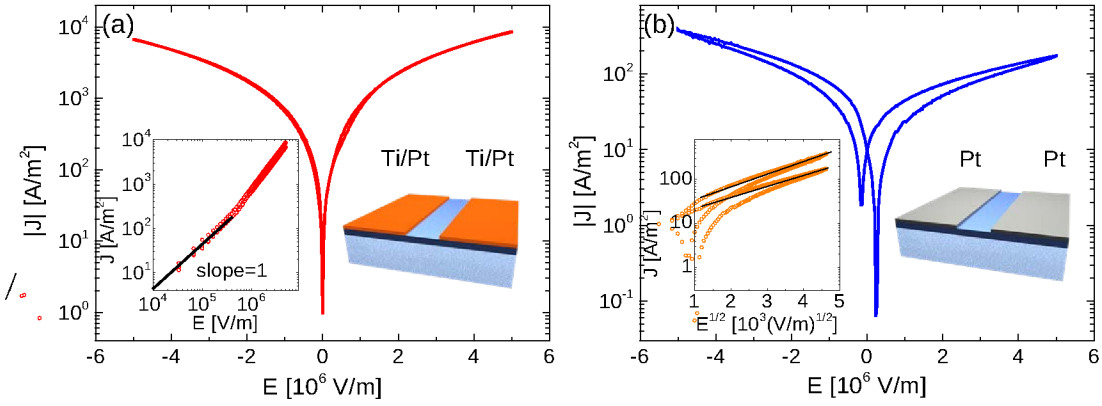


*Figure 4: IVCs of a 90 nm thick strained $SrTiO_3$ film measured with two parallel oriented electrodes (gap size 3 µm and length 500 µm) for (a) Ti/Pt electrodes and (b) Pt electrodes measured at room temperature. The inserts represent a double-logarithmic plot (a) and a Schottky fit (b) of the IVCs.*

Fig. 4 shows a comparison of typical current-voltage characteristics (IVCs) of metal-insulator-metal structures obtained for a combination of Pt or Ti/Pt electrodes with a strained $SrTiO_3$ film. The measurements are performed at room temperature in order to obtain the conductivity of the oxide film at operation temperature. Again a rather large gap of 3 μm has been chosen which is compensated by the large length (500 μm) of the electrodes. The main features of this experiment are:

(i) The Ti/Pt electrodes lead to a much larger conductivity compared to the device with pure Pt electrode. This is most likely caused by the high density of oxygen vacancies at the Ti-$SrTiO_3$ interface, which reduce the barrier height of the metal-oxide interface.[14, 39]

(ii) Furthermore, the two devices show a different conduction mechanism. Whereas the Ti-$SrTiO_3$ interface behaves ohmic as indicated by the linear part of the IVC at low electric fields (see insert of Fig. 4(a)), we observe a Schottky behavior according to $\ln J \propto \sqrt{E}$ for the Pt-$SrTiO_3$ interface (see insert of Fig. 4(b)).

Although in other reports the electrodes showing Schottky behavior have been utilized to establish a memristor [34, 40, 41], in this work we use the ohmic behavior (at small electric fields) of the Ti-$SrTiO_3$ interface in combination with (i) the strain enhanced conductivity and (ii) an asymmetric electrode concept. Using the strained $SrTiO_3$ films on (110) $DyScO_3$ in combination with a combination of a flat and a tapered electrode we developed planar memristors that show the desired plastic behavior, i.e. the desired behavior of an e-synapse.

### C. E-synapse made from strained $SrTiO_3$

Fig. 5 shows typical results obtained for asymmetric electrode designs consisting of a sharp tip opposing a flat electrode (see sketch in Fig. 5(a)). The distance between both electrodes is 500 nm, the sharpness of the tip is 14°. Fig. 5(a) shows the memristor behavior as well as the plasticity which both are essential characteristics of an e-synapse. In this measurement a continuous voltage sweep is applied at the electrodes, the values next to the curves indicate the number of the successive voltage cycle (not all cycles are shown). The IVCs show the typical memristor behavior with a high current (conductance) in the ON

state and a low current (conductance) in the OFF state. However, while the OFF state stays low, the ON state increases with increasing number of cycles (shown for a read voltage of 5 V in Fig. 5(b)). This plastic behavior is know from literature [42]. It represents a gradual process defined by the migration of oxygen vacancies (see sketches in Fig. 5). In the beginning the vacancies form very thin channels that allow only a small transport current. With each loop the channels grow wider until the local electrical field gradient becomes too weak to support any further migration of oxygen vacancies. The role of the electric field and the resulting local temperature for the migration of the oxygen vacancies will be discussed later. First indications on the internal dynamics, i.e. motion of oxygen vacancies, and resulting conducting mechanisms can be obtained from the IVCs (see Fig. 5(c) and (d)).

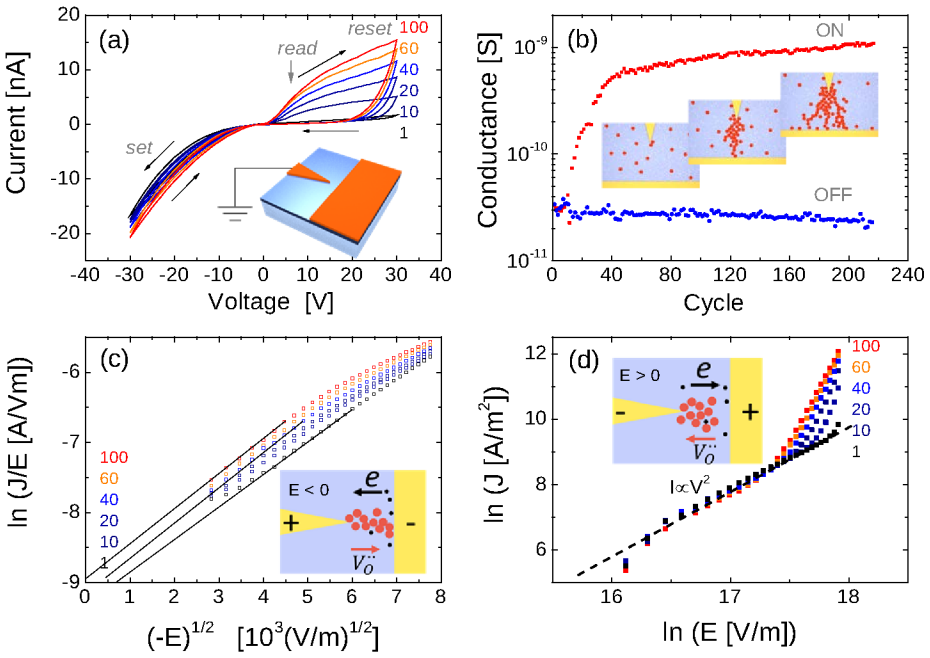


*Figure 5: IVCs of an asymmetric pair of Ti/Pt electrodes consisting of a flat electrode (500 µm wide) and a tapered (14°) electrode at a distance of 500 nm (sketch in (a)) on a 90 nm thick strained $SrTiO_3$ film on $DyScO_3$. (a) Series of subsequently recorded IVCs demonstrating the e-synaptic behavior, the numbers indicate the number of cycles, the positions for set, reset, and read are indicated. (b) Time dependence of the read signal recorded at a read voltage of 5 V for the ON state (red symbols) and OFF state (blue state)*

*using the data in (a). (c) Poole–Frenkel emission fit of the reverse bias, and (d) double logarithmic plot of the OFF state plot with an initial slope of ~2 indicating a trap controlled space-charge-limited behavior of the low conductivity state. The sketches in the figure show the electrode geometry (a) or the expected distribution of oxygen vacancies (red dots) in (b, c, and d).*

For negative voltages ("set voltage", electrons move from the flat electrode towards the tip) a Poole-Frenkel (PF) behavior [43, 44] is observed (Fig. 5(c)). The PF emission describes a hopping of electrons in an electrical insulator. Electrons are trapped in localized states. Due to thermal fluctuation they can spontaneously be excited to the conduction band and move (hop) under the impact of an electric field to another trapping side. For large electric fields this leads to a current density *J*:

$$J = q\mu E n_0 \exp\left[-\frac{q\phi_B}{kT} + \frac{q}{kT}\left(\frac{qE}{\pi\varepsilon\varepsilon_0}\right)^{1/2}\right] \qquad (2)$$

where $q$ is the electron charge, $\mu$ is the electronic drift mobility, $n_0$ is the density of electrons in the conduction band (here the defect concentration), $\phi_B$ is the voltage barrier for the hopping of electrons trapped in an isolator, and ε is the dielectric constant of the isolator.

Fig. 5(c) shows a typical PF behavior, i.e. a linear correlation between ln(J/E) and $E^{1/2}$ in agreement with eq. (2). Using typical values $\mu = 0.4 \cdot 10^{-4}$ $m^2V^{-1}s^{-1}$ for the mobility and $n_0 = 1.5 \cdot 10^{24}$ $m^{-3}$ for the initial electron density in $SrTiO_3$,[45] we obtain a reasonable value of $\phi_B \cong 0.28$ eV which describes the voltage barrier that the electrons have to overcome in order to hop between defects in our strained $SrTiO_3$. With increasing number of voltage cycles the height of the linear PF fit changes slightly (see Fig. 5(c)). In terms of the PF model this implies that with increasing number of voltage cycles either the electron concentration $n_0$ increases or the voltage barrier $\phi_B$ decreases. Since we can assume that the height of the voltage barrier is a characteristic property of the defects (oxygen vacancies) in our strained $SrTiO_3$ which should not be affected by the voltage cycles, the density $n_0$ or distribution of the defects between the two electrodes has to change due to

the voltage cycles. This agrees with the general picture shown in Fig. 5(b) and (c). Electrons hop from defects (oxygen vacancies) to defect. With increasing number of cycles more percolative defect channels are formed between both electrodes which automatically affects the effective density of defects between the electrodes. According to the PF model, the charge carrier density would increase by ~67% during the first 100 voltage cycles shown in Fig. 5. This increase is most likely the result of redox processes in the $SrTiO_3$ film [7, 46, 47].

For positive voltages ("read" and "reset") electrons move from the tip to the flat electrode (see sketch in Fig. 5(d)). First a large conductivity marks the ON state of the e-synapse. However, at high enough voltages oxygen vacancies are pushed away from the flat electrode, which will causes a disruption of the conductive defect channels ("reset"). This gaps strongly reduce the conductance of the e-synapse resulting in the low conducting OFF state. In the OFF state the IVCs show no plasticity. Moreover, they display the expected space-charge-limited current with the characteristic $I \propto V^{1/2}$ (see Fig. 5(d)) [48].

In order to understand the impact of the electrode geometry on the electric field and resulting temperature distribution during the electroforming process, different electrode designs were analyzed. In all cases designs similar to that of the experiments were chosen, i.e. a sharp tip opposing a flat electrode with a distance between the electrodes of 500 nm. However the sharpness (i.e. angle) of the tip was varied. Due to the relatively large gap between the two electrodes (tip and flat electrode) the diameter of the very tip can be neglected. First, a 2-D electric field distribution was calculated via finite-difference time-domain (FDTD) method [49] assuming a homogeneous thin $SrTiO_3$ layer. A typical example of the initial field distribution is shown in Fig. 6(a). Generally the field gradient is largest at the tip of the tapered electrode. This gradient increases with the sharpness of the tip, i.e. with decreasing angle that describes the tapered geometry. The electric field gradient leads to a current and, thus, to a local heating of the film. Both, electric field and the thermal effect, determine the drift of oxygen vacancy, i.e. the electroforming process.

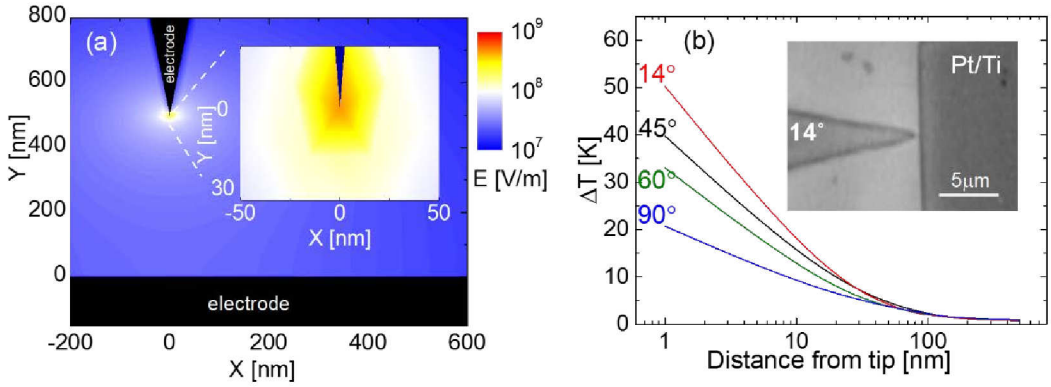


*Figure 6: (a) 2D initial electric field distribution for a 14° tip and (b) resulting change of the temperature as function of distance from the tip in the direction to the flat electrode for different angles of the tapered electrode. The applied voltage is 30 V, the inset in (b) shows an image of a real electrode with a 14° tip.*

For the evaluation of the resulting temperature distribution in the initial state of the device, we consider an electronic heating of the $SrTiO_3$ between the electrodes and a cooling provided by the substrate. All other thermal effects can be negligible. On the one hand the thermal energy induced by a current in a small volume V is:

$$Q_{in} = I^2 \mathrm{Rt} = \mathrm{cm}\Delta\mathrm{T} \qquad (3)$$

where $I$ is the current flowing through volume V, R and m are resistance and mass of V, c is the specific heat of $SrTiO_3$, t is the duration of the current pulse, and ΔT is the resulting change in temperature. On the other hand, the heat flow through an area $a^2$ at the interface between film and substrate is:

$$Q_{out} = k\, a^2\, \frac{T_{surface} - T_{substrate}}{h} t \qquad (4)$$

where $k$ is the thermal conductivity and $h$ represents the thickness of the film. Inserting reasonable values for our $SrTiO_3$ films, e.g. c = 30 cal/mol·K [50], and $k$ = 6 W/(m·K) [51], we can evaluate the time $\tau$ after which the temperature in the $SrTiO_3$ film is stable (here other effects like the plasticity, i.e. migration of oxygen vacancies, are not

considered). Assuming $Q_{in} = Q_{out}$ in the stable state, we obtain a value $\tau \leq 5$ µs for our $SrTiO_3$ films of thickness $h < 100$ nm. This means that after an extremely short time of only a few microseconds, a stable temperature distributation is obtained during electroformation or pulse experiments in our $SrTiO_3$ film.

With this knowledge and the assumption that the substrate represents a large heat sink at a constant temperature (i.e. room temperature), we can even obtain the temperature distribution in the first microseconds of a current pulse using eq. (4) and (5). Fig. 6(b) shows the change of temperature in the in-plane direction pointing from the tip of the tapered electrode to the flat electrode. Generally the temperature increase peaks at the tip and reduces strongly with the distance to the tip. With increasing sharpness of the tip ΔT increases. Consequently, sharp tips were chosen for the experiment which at the same time are technically feasible and robust. The best results were obtained for the sharpest tip with an angle of 14° (see Fig. 6(b)), smaller angles were not examined.

The major component of the initial electroformation and the following operation of our e-synapse is the migration of oxygen vacancy in the $SrTiO_3$ layer. This migration is caused by the combined action of the local electric field and temperature. In the regular lattice of the ionic $SrTiO_3$, oxygen vacancies are positively charged. Under a large enough electric field, the oxygen vacancies tend to move towards the negatively charged electrode. At the same time, the electric field leads to a local heating which enables or enhances the mobility of the oxygen vacancies [52]. Initially the highest mobility is expected at the positively charged electrode (e.g. the sharp tip in the set state). With the formation of the channel this point of highest electric field and, thus, highest temperature moves with the channel front towards the negatively charged electrode. Due to the asymmetric design of the electrodes, this process of electroformation of conductive channels is fastest for the development of channels from the sharp tip to the flat electrode (see sketches in Fig. 5). Once a conductance channel is completed, the electric field becomes homogeneous and further migration is stopped, the initial electroformation is finished.

The drift velocity of the oxygen vacancies can be described by the Mott-Gurney equation [38]:

$$v = dfexp(-\frac{E_A}{kT})\sinh(\frac{zd}{2kT}E) \quad (5)$$

where $d$ represents the hopping distance, $f$ is the attempt frequency, $E_A$ is the activation energy, $z$ is the charge of the ion, and $E$ is the electric field. Inserting reasonable values, e.g. d = 4 Å for $SrTiO_3$, $z = 2$ for double positively charged oxygen vacancies, an attempt frequency $f = 6.67 \times 10^{12}$ Hz [38], and activation energy of oxygen vacancy of 0.8 eV and 0.7 eV for unstrained and tensile strained $SrTiO_3$ [24], we can simulated the mobility of oxygen vacancies in unstrained and strained $SrTiO_3$ as function of electric field and temperature.

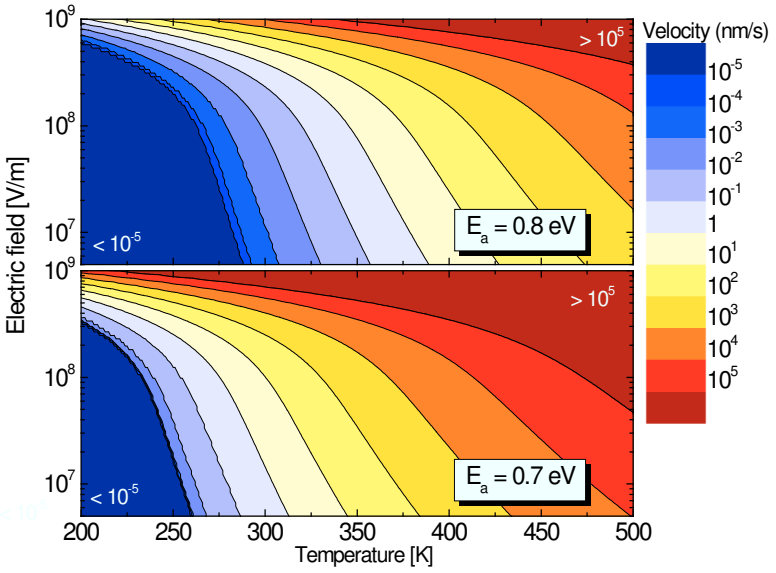


*Figure 7: 2-D contour plots of the drift velocity of oxygen vacancy according to eq. (5) using activation energies of 0.8 and 0.7 eV for unstrained and tensile strained $SrTiO_3$, respectively.*

The resulting comparison of the drift velocities for strained and unstrained $SrTiO_3$ (see Fig. 7) provide a number of interesting information. First, the oxygen vacancy mobility is generally higher in strained $SrTiO_3$ compared to unstrained $SrTiO_3$. From our FDTD simulation (see e.g. Fig. 6a) we know, that in our experiments (voltages clearly below 30 V) the typical electric field between the two electrodes ranges between ~$10^7$ and ~$2 \cdot 10^8$ V/m. Already at room temperature, the velocity of oxygen vacancies is of the order of 1 to

10 nm/s for strained $SrTiO_3$, which is 10 to 100 times faster than for unstrained $SrTiO_3$. Second, the mobility is locally further enhanced due to the local heating of the $SrTiO_3$. As shown in Fig. 6b, the local temperature can easily be enhanced by several tens of K at the sharp tip, e.g. 50 K for our 14° tip (see Fig. 6). Due to this temperature increase, the velocity of oxygen vacancy migration is further enhanced at the position of the highest field gradient. These considerations reveal that the combination of strained $SrTiO_3$ and an optimized electrode design (sharp tip and a flat electrode) lead to a high mobility of the oxygen vacancies. However, too large mobility can be detrimental on even destructive for the device. This can be demonstrated by enhancing either the temperature of the device or the electric field during the experiment.

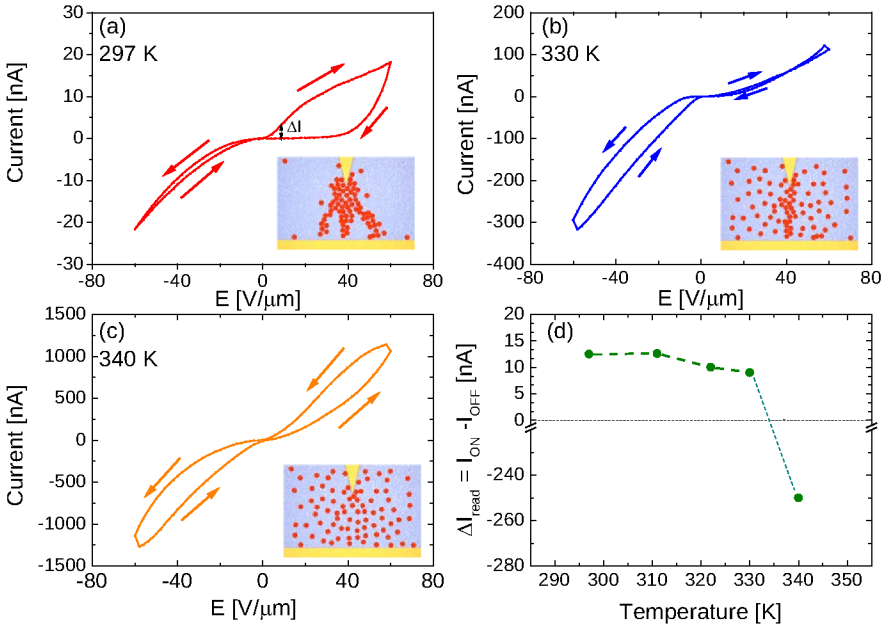


*Figure 8: (a-c) IVCs of an e-synapse (14° tip) on 90nm thick $SrTiO_3$ film on $DyScO_3$ measured at different temperatures and (d) difference of the read current measured at 5V in the ON state and OFF state. The schematics in (a-c) display the expected change of the distribution of oxygen vacancies for the different temperatures.*

Fig. 8 shows a series of IVCs taken at different temperatures. Starting after electro-formation at room temperature (Fig. 8(a)) one obtains a perfect memristor behavior which

has already been discussed in detail in Fig. 5. By increasing the temperature to 330 K (Fig. 8(b)) the conductivity increases by a factor ~4 (reset) or ~10 (set), whereas the hysteresis in the positive voltage regime is slightly reduced, e.g. the difference of the read signal ($\Delta I_{read}=I_{ON}-I_{OFF}$) in the ON state and OFF state is reduced by ~30% (see Fig. 8(d)). A further enhancement of the temperature to 340 K (Fig. 8(c)), leads to a strong enhancement of the conductivity by more than an order of magnitude and an inversion of the hysteresis in the positive voltage regime. The IVC is nearly symmetric, $\Delta I_{read}$ is now negative (see Fig. 8d) and the device does not operate as a memristor or even e-synapse anymore. The enhancement of the operating temperature from room temperature to 340 K completely changes the behavior of the device. The resulting changeover of the difference of the read current $\Delta I_{read}$ in the ON and OFF state from positive to negative is summarized in Fig. 8(d).

### D. Plasticity of E-synapse made from strained $SrTiO_3$

In order to examine the plastically of our e-synapse, we performed various series of pulse measurements. These measurements should demonstrate the ability of these devices to "learn" and "forget" similar to the synaptic long-term and short-term potentiation/depression or spike-time-dependent plasticity.

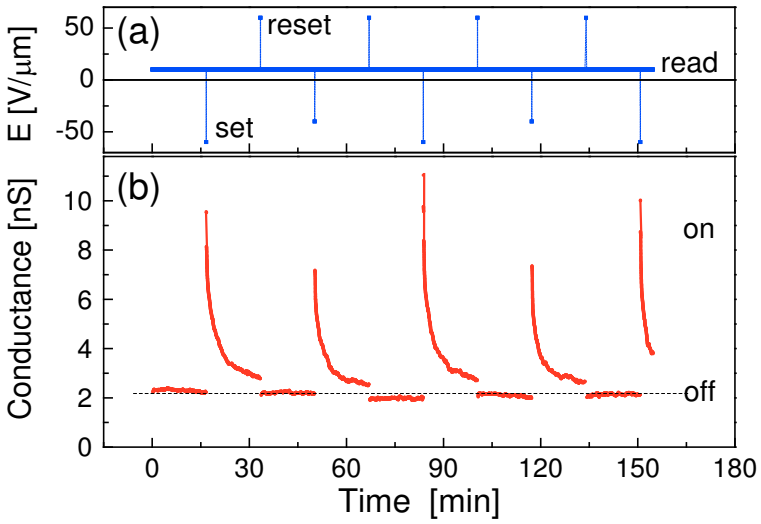


*Figure 9: (a) Train of voltage pulses consisting of reset pulses (+60 V/µm, 5 s), set pulses (-60 V/µm, 5 s and -20 V/µm, 5 s), and a read electric field of 10 V/µm and (b) resulting*

*read conductance measured from an e-synapse (14° tip and 90 nm thick strained $SrTiO_3$ on $DyScO_3$).*

Fig. 9 shows a typical result obtained for our e-synapse for a series of set-pulses of different height. The electric fields are subsequently -60 V/µm and -40 V/µm for $E_{set}$, 60 V/µm for $E_{reset}$, and 10 V/µm for $E_{read}$. The resulting read conductance is unchanged at ~2 nS for the OFF state, whereas it relaxes strongly in the ON state.

Generally the initial height of the ON state conductance should depends on:

(i) the starting point, i.e. the read conductance at which we start the series (history effect),

(ii) the amplitude of the set field $E_{set}$,

(iii) the duration of the set-pulse, and

(iv) the repetition rate of the set-pulse.

In the experiment shown in Fig. 9, only $E_{set}$ is varied. For the larger $E_{set}$ (1st, 3rd, and 5th pulse) a large initial signal is recorded directly after the set pulse. However the subsequent relaxation of the signal in the read state looks very similar for all pulses (small and large $E_{set}$).

The relaxation of the signal follows the classical relaxation process described by a Kohlrausch-Williams-Watts function [53]:

$$I(t) \propto exp\left[-\left(\frac{t}{\tau}\right)^{\beta}\right] \qquad (6)$$

where $\beta$ represents the coupling parameter (typically $0 < \beta < 1$) and $\tau$ is the mean relaxation time. All relaxation processes of the ON state shown in Fig. 9 can be fitted by eq.(6) yielding values of $\beta \cong 0.17$ and $\tau \cong 10$ s. The resulting exponent $\beta \cong 0.17$ indicates that the distribution of the local conductance is inhomogeneous (a $\beta$ value close to 0 is an indication for an inhomogeneous distribution). The mean relaxation time $\tau \cong 10$ s is reasonable since the mobility of oxygen vacancies in the nano gap between the electrodes is estimated to be below 10 nm/s (see Fig. 7).

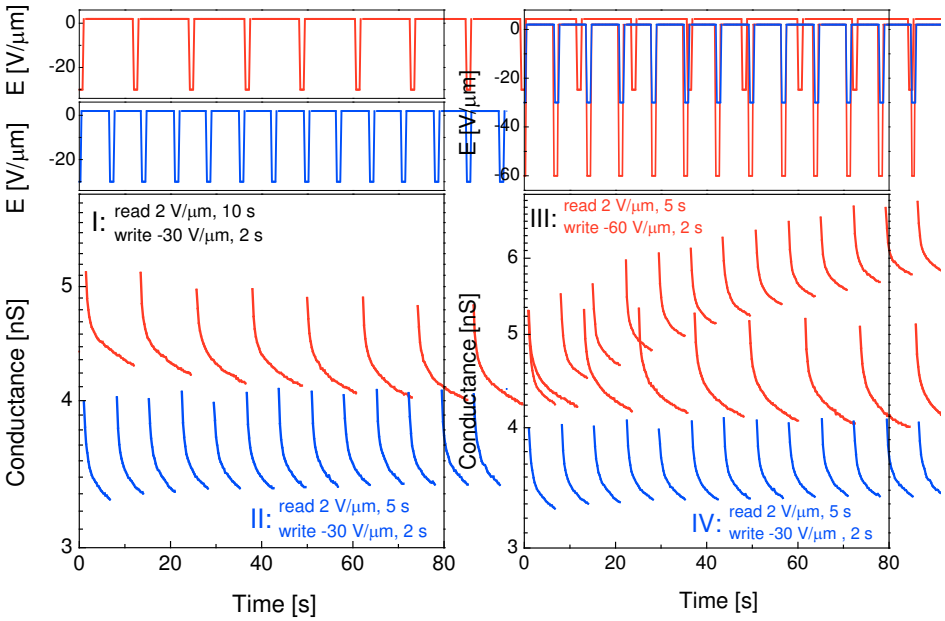


*Figure 10: Relaxation of the conductance in the read state for various series of electric set-pulses varying the frequency (left, series I and II) or amplitude (right, series III and IV) of the stimulus. The top shows the two different set pulses (blue and red), the resulting read conduction is given in the figures below using the same color code.*

Fig. 10 demonstrates the short-term plasticity of the e-synapse. It shows 4 different series of measurements where the frequency and amplitude of the set-pulses are varied. Moreover, different starting conditions are chosen. In all cases we observe the characteristic relaxation of the ON state signal similar to that shown in Fig. 9. In the left set, the frequency of the set pulses is changed, amplitude and pulse duration are identical. For the larger frequency a small increase of the general signal height is observed, whereas for the smaller frequency the general signal height decreases. For the right set, the amplitude of the set pulses is modified, frequency and duration are identical. Whereas the signal level is nearly unchanged in case of the smaller set amplitude, it increases strongly for the large set amplitude. In conclusion of the experiments shown in Fig. 10, the general trend of the ON-state signal height show a clearly visible dependence on the amplitude, duration and repetition rate of the set pulse.

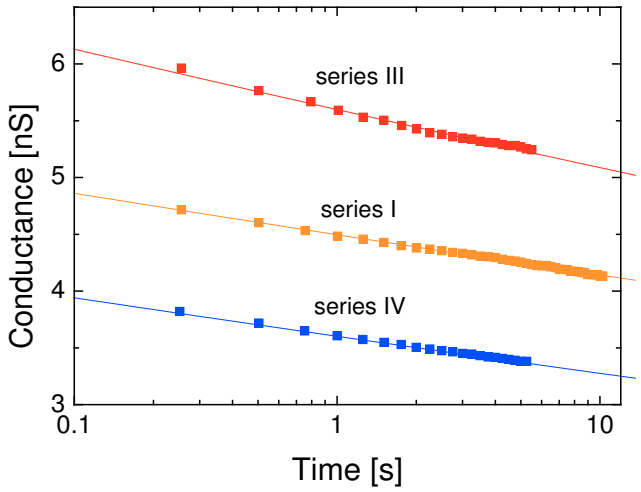


*Figure 11: Typical fit of the relaxation of the read conductance after a set pulse according to eq. (6). The data represent different series shown in Fig. 10, in all cases a relaxation time $\tau \cong 100$ ps and a coupling parameter $\beta \cong 0.022$ is obtained.*

However, as demonstrated in the semilogarithmic plot of the first seconds (Fig. 11), all relaxation processes show the same stretched exponential behavior of eq. (6). There is no significant difference for the different types of reset pulses. The small exponent $\beta \cong 0.022$ indicates that there is only a small coupling in the system due to a highly inhomogeneous distribution of the local conductance. The mean relaxation time $\tau \cong 100$ ps corresponds to a frequency of ~ 10 GHz which is characteristic for the limiting frequency of dipole motion in ionic oxide crystals [54].

In the end we can identify two types of processes that cause the plasticity in our $SrTiO_3$ e-synapse:

(i) A fast process defined by the ionic dipole formation (polarization) in the strained $SrTiO_3$ leads to a fast relaxation with a mean relaxation time of $\tau \cong$ 100 ps.

(ii) A slow process defined by the mobility of oxygen vacancies with a mean relaxation time of $\tau \cong 10$ s at room temperature. The latter process represents

depends on the amplitude, duration, repetition rate of the set and reset pulses as well as on the initial state of the synapse.

## Conclusions

In this work we engineer the electronic transport properties of $SrTiO_3$ thin film via epitaxial strain and demonstrate that strain-optimized $SrTiO_3$ layers might be used as the active component in artificial synaptic devices (e-synapse). Using the tensile strain imposed by the rare-earth scandate substrates on epitaxial grown $SrTiO_3$ films, we not only enhance the density and mobility of oxygen vacancies in the film but also shift the ferroelectric-paraelectric phase transition to room temperature. As a result the conductivity of the $SrTiO_3$ increases by orders of magnitude (e.g. from $\sim 10^{-6}$ S/m to $>10^{-4}$ S/m for unstrained and strained $SrTiO_3$, respectively), we observe a significant plasticity of the conductivity, and due to the phase transition close to room temperature (operating temperature) we expect a high stability (robustness) of an e-synapse made from these films. A further enhancement of the conductivity is obtained by the use of Ti/Pt electrodes. In contrast to pure Pt electrodes which show a Schottky behavior and which are usually used in memristor devices [34, 40, 41], we utilize the ohmic behavior of the Ti-$SrTiO_3$ interface in combination with asymmetric electrodes for the demonstration of planar arranged e-synapse.

The resulting e-synapses show memristor behavior as well as the plasticity of the signal which both are essential characteristics of an e-synapse. Our experiments demonstrate the ability of these devices to “learn” and “forget”. Similar to the synaptic long-term and short-term potentiation/depression or spike-time-dependent plasticity [45], two different types of plasticity can be identified for our $SrTiO_3$ e-synapse: a fast process associated with the ionic dipole formation and a relaxation time in the 100 ps regime and a slow process defined by the mobility of oxygen vacancies with a relaxation time of several seconds. Considering the stability and flexibility of these planar devices we believe that strain-engineered $SrTiO_3$ or alternative oxides might provide extremely interesting opportunities for the development of many low-power e-synaptic device concepts.

**Acknowledgement:**

The authors would like to thank A. Offenhäusser, D. Mayer, J. Schwarzkopf, R. Kutzner, W. Zander, T. Grellmann, K. Greben, B. Cai, and A. Markov for their valuable discussions and technical support. Financial support from the China Scholarship Council (Grant number 201306280005) is also gratefully acknowledged.

**Reference**

1. Krogh, A., *What are artificial neural networks?* Nature biotechnology, 2008. **26**(2): p. 195-197.
2. Silver, D., A. Huang, C.J. Maddison, A. Guez, L. Sifre, G. van den Driessche, J. Schrittwieser, I. Antonoglou, V. Panneershelvam, M. Lanctot, S. Dieleman, D. Grewe, J. Nham, N. Kalchbrenner, I. Sutskever, T. Lillicrap, M. Leach, K. Kavukcuoglu, T. Graepel, and D. Hassabis, *Mastering the game of Go with deep neural networks and tree search.* Nature, 2016. **529**(7587): p. 484-+.
3. Hu, M., C.E. Graves, C. Li, Y.N. Li, N. Ge, E. Montgomery, N. Davila, H. Jiang, R.S. Williams, J.J.S. Yang, Q.F. Xia, and J.P. Strachan, *Memristor-Based Analog Computation and Neural Network Classification with a Dot Product Engine.* Advanced Materials, 2018. **30**(9).
4. Ziegler, M., C. Wenger, E. Chicca, and H. Kohlstedt, *Tutorial: Concepts for closely mimicking biological learning with memristive devices: Principles to emulate cellular forms of learning.* Journal of Applied Physics, 2018. **124**(15).
5. Jo, S.H., T. Chang, I. Ebong, B.B. Bhadviya, P. Mazumder, and W. Lu, *Nanoscale memristor device as synapse in neuromorphic systems.* Nano Lett, 2010. **10**(4): p. 1297-1301.
6. Zhu, X.J. and W.D. Lu, *Optogenetics-Inspired Tunable Synaptic Functions in Memristors.* ACS nano, 2018. **12**(2): p. 1242-1249.
7. Heisig, T., C. Baeumer, U.N. Gries, M.P. Mueller, C. La Torre, M. Luebben, N. Raab, H.C. Du, S. Menzel, D.N. Mueller, C.L. Jia, J. Mayer, R. Waser, I. Valov, R.A. De Souza, and R. Dittmann, *Oxygen Exchange Processes between Oxide Memristive Devices and Water Molecules.* Advanced Materials, 2018. **30**(29).
8. Wedig, A., M. Luebben, D.Y. Cho, M. Moors, K. Skaja, V. Rana, T. Hasegawa, K.K. Adepalli, B. Yildiz, R. Waser, and I. Valov, *Nanoscale cation motion in $TaO_x$, $HfO_x$ and $TiO_x$ memristive systems.* Nat Nanotechnol, 2016. **11**(1): p. 67-+.
9. Driscoll, T., H.T. Kim, B.G. Chae, M. Di Ventra, and D.N. Basov, *Phase-transition driven memristive system.* Applied Physics Letters, 2009. **95**(4).
10. Chanthbouala, A., V. Garcia, R.O. Cherifi, K. Bouzehouane, S. Fusil, X. Moya, S. Xavier, H. Yamada, C. Deranlot, N.D. Mathur, M. Bibes, A. Barthelemy, and J. Grollier, *A ferroelectric memristor.* Nat Mater, 2012. **11**(10): p. 860-4.
11. Tian, B., L. Liu, M. Yan, J. Wang, Q. Zhao, N. Zhong, P. Xiang, L. Sun, H. Peng, H. Shen, T. Lin, B. Dkhil, X. Meng, J. Chu, X. Tang, and C. Duan, *A Robust Artificial Synapse*

*Based on Organic Ferroelectric Polymer.* Advanced Electronic Materials, 2019. **5**(1): p. 1800600.
12. Kim, K.M., D.S. Jeong, and C.S. Hwang, *Nanofilamentary resistive switching in binary oxide system; a review on the present statusand outlook.* Nanotechnology, 2011. **22**(25): p. 254002.
13. Kim, D.C., S. Seo, S.E. Ahn, D.S. Suh, M.J. Lee, B.H. Park, I.K. Yoo, I.G. Baek, H.J. Kim, E.K. Yim, J.E. Lee, S.O. Park, H.S. Kim, U.I. Chung, J.T. Moon, and B.I. Ryu, *Electrical observations of filamentary conductions for the resistive memory switching in NiO films.* Applied Physics Letters, 2006. **88**(20).
14. Yang, J.J., M.D. Pickett, X. Li, D.A. Ohlberg, D.R. Stewart, and R.S. Williams, *Memristive switching mechanism for metal/oxide/metal nanodevices.* Nat Nanotechnol, 2008. **3**(7): p. 429-33.
15. Yin, X.B., R. Yang, K.H. Xue, Z.H. Tan, X.D. Zhang, X.S. Miao, and X. Guo, *Mimicking the brain functions of learning, forgetting and explicit/implicit memories with $SrTiO_3$-based memristive devices.* Physical Chemistry Chemical Physics, 2016. **18**(46): p. 31796-31802.
16. Funck, C., A. Marchewka, C. Bäumer, P.C. Schmidt, P. Müller, R. Dittmann, M. Martin, R. Waser, and S. Menzel, *A Theoretical and Experimental View on the Temperature Dependence of the Electronic Conduction through a Schottky Barrier in a Resistively Switching $SrTiO_3$-Based Memory Cell.* Advanced Electronic Materials, 2018. **4**(7): p. 1800062.
17. Shuai, Y., S. Zhou, D. Bürger, M. Helm, and H. Schmidt, *Nonvolatile bipolar resistive switching in Au/$BiFeO_3$/Pt.* Journal of Applied Physics, 2011. **109**(12): p. 124117.
18. Janousch, M., G.I. Meijer, U. Staub, B. Delley, S.F. Karg, and B.P. Andreasson, *Role of oxygen vacancies in Cr ‐ doped $SrTiO_3$ for resistance ‐ change memory.* Advanced Materials, 2007. **19**(17): p. 2232-2235.
19. Ohly, C., S. Hoffmann-Eifert, X. Guo, J. Schubert, and R. Waser, *Electrical Conductivity of Epitaxial $SrTiO_3$ Thin Films as a Function of Oxygen Partial Pressure and Temperature.* Journal of the American Ceramic Society, 2006. **89**(9): p. 2845-2852.
20. Szot, K., W. Speier, G. Bihlmayer, and R. Waser, *Switching the electrical resistance of individual dislocations in single-crystalline $SrTiO_3$.* Nat Mater, 2006. **5**(4): p. 312-20.
21. Wong, F.J., S.-H. Baek, R.V. Chopdekar, V.V. Mehta, H.-W. Jang, C.-B. Eom, and Y. Suzuki, *Metallicity in$LaTiO_3$ thin films induced by lattice deformation.* Physical Review B, 2010. **81**(16).
22. Wang, B., L. You, P. Ren, X. Yin, Y. Peng, B. Xia, L. Wang, X. Yu, S.M. Poh, P. Yang, G. Yuan, L. Chen, A. Rusydi, and J. Wang, *Oxygen-driven anisotropic transport in ultra-thin manganite films.* Nat Commun, 2013. **4**: p. 2778.
23. Dai, Y., J. Schubert, E. Hollmann, G. Mussler, and R. Wördenweber, *Engineering of the Curie temperature of epitaxial $Sr_{1-x}Ba_xTiO_3$ films via strain.* Journal of Applied Physics, 2016. **120**(11): p. 114101.
24. Al-Hamadany, R., J.P. Goss, P.R. Briddon, S.A. Mojarad, A.G. O'Neill, and M.J. Rayson, *Impact of tensile strain on the oxygen vacancy migration in $SrTiO_3$: Density functional theory calculations.* Journal of Applied Physics, 2013. **113**(22): p. 224108.
25. Haeni, J., P. Irvin, W. Chang, R. Uecker, P. Reiche, Y. Li, S. Choudhury, W. Tian, M. Hawley, and B. Craigo, *Room-temperature ferroelectricity in strained $SrTiO_3$.* Nature, 2004. **430**(7001): p. 758-761.
26. Hilton, A. and B. Ricketts, *Dielectric properties of ceramics.* Journal of Physics D: Applied Physics, 1996. **29**(5): p. 1321.
27. Kvasov, A. and A.K. Tagantsev, *Positive effective $Q_{12}$ electrostrictive coefficient in perovskites.* Journal of Applied Physics, 2012. **112**(9): p. 094106.

28. Kityk, A., W. Schranz, P. Sondergeld, D. Havlik, E. Salje, and J. Scott, *Low-frequency superelasticity and nonlinear elastic behavior of $SrTiO_3$ crystals.* Physical Review B, 2000. **61**(2): p. 946.
29. Albrecht, W., J. Moers, and B. Hermanns, *HNF - Helmholtz Nano Facility.* Journal of large-scale research facilities JLSRF, 2017. **3**(A112).
30. Peng, H.Y., L. Pu, J.C. Wu, D. Cha, J.H. Hong, W.N. Lin, Y.Y. Li, J.F. Ding, A. David, K. Li, and T. Wu, *Effects of electrode material and configuration on the characteristics of planar resistive switching devices.* APL Materials, 2013. **1**(5): p. 052106.
31. Choi, S.Y., S.D. Kim, M. Choi, H.S. Lee, J. Ryu, N. Shibata, T. Mizoguchi, E. Tochigi, T. Yamamoto, S.J. Kang, and Y. Ikuhara, *Assessment of Strain-Generated Oxygen Vacancies Using $SrTiO_3$ Bicrystals.* Nano Lett, 2015. **15**(6): p. 4129-34.
32. Bock, J.A., S. Lee, S. Trolier-McKinstry, and C.A. Randall, *Metallic-like to nonmetallic transitions in a variety of heavily oxygen deficient ferroelectrics.* Applied Physics Letters, 2015. **107**(9): p. 092902.
33. Tiwari, A., C. Jin, and J. Narayan, *Strain-induced tuning of metal–insulator transition in $NdNiO_3$.* Applied Physics Letters, 2002. **80**(21): p. 4039-4041.
34. Mikheev, E., B.D. Hoskins, D.B. Strukov, and S. Stemmer, *Resistive switching and its suppression in Pt/Nb:$SrTiO_3$ junctions.* Nat Commun, 2014. **5**: p. 3990.
35. Abe, K. and S. Komatsu, *Epitaxial growth of $SrTiO_3$ films on Pt electrodes and their electrical properties.* Japanese Journal of Applied Physics, 1992. **31**(9S): p. 2985.
36. Shen, J., H. Lee, R. Valentí, and H.O. Jeschke, *Ab initiostudy of the two-dimensional metallic state at the surface of $SrTiO_3$: Importance of oxygen vacancies.* Physical Review B, 2012. **86**(19).
37. Kubicek, M., R. Schmitt, F. Messerschmitt, and J.L. Rupp, *Uncovering two competing switching mechanisms for epitaxial and ultrathin strontium titanate-based resistive switching bits.* ACS nano, 2015. **9**(11): p. 10737-10748.
38. Starschich, S., S. Menzel, and U. Böttger, *Evidence for oxygen vacancies movement during wake-up in ferroelectric hafnium oxide.* Applied Physics Letters, 2016. **108**(3): p. 032903.
39. Joshua Yang, J., F. Miao, M.D. Pickett, D.A. Ohlberg, D.R. Stewart, C.N. Lau, and R.S. Williams, *The mechanism of electroforming of metal oxide memristive switches.* Nanotechnology, 2009. **20**(21): p. 215201.
40. Kan, D. and Y. Shimakawa, *Transient behavior in Pt/Nb-doped $SrTiO_3$ Schottky junctions.* Applied Physics Letters, 2013. **103**(14): p. 142910.
41. Miao, F., J. Joshua Yang, J. Borghetti, G. Medeiros-Ribeiro, and R. Stanley Williams, *Observation of two resistance switching modes in $TiO_2$ memristive devices electroformed at low current.* Nanotechnology, 2011. **22**(25): p. 254007.
42. Yang, R., K. Terabe, Y. Yao, T. Tsuruoka, T. Hasegawa, J.K. Gimzewski, and M. Aono, *Synaptic plasticity and memory functions achieved in a $WO_{3-x}$-based nanoionics device by using the principle of atomic switch operation.* Nanotechnology, 2013. **24**(38): p. 384003.
43. Kao, K.C., *Dielectric phenomena in solids*. 2004: Academic press.
44. Mojarad, S.A., K.S.K. Kwa, J.P. Goss, Z. Zhou, N.K. Ponon, D.J.R. Appleby, R.A.S. Al-Hamadany, and A. Oneill, *A comprehensive study on the leakage current mechanisms of Pt/$SrTiO_3$/Pt capacitor.* Journal of Applied Physics, 2012. **111**(1): p. 1032.
45. Ambwani, P., P. Xu, G. Haugstad, J.S. Jeong, R. Deng, K.A. Mkhoyan, B. Jalan, and C. Leighton, *Defects, stoichiometry, and electronic transport in $SrTiO_{3-\delta}$ epilayers: A high pressure oxygen sputter deposition study.* Journal of Applied Physics, 2016. **120**(5): p. 055704.
46. Dittmann, R., R. Muenstermann, I. Krug, D. Park, T. Menke, J. Mayer, A. Besmehn, F. Kronast, C.M. Schneider, and R. Waser, *Scaling Potential of Local Redox Processes in Memristive $SrTiO_3$ Thin-Film Devices.* Proceedings of the IEEE, 2012. **100**(6): p. 1979-1990.

47. Du, H.C., C.L. Jia, A. Koehl, J. Barthel, R. Dittmann, R. Waser, and J. Mayer, *Nanosized Conducting Filaments Formed by Atomic-Scale Defects in Redox-Based Resistive Switching Memories.* Chemistry of Materials, 2017. **29**(7): p. 3164-3173.
48. Sangwan, V.K., D. Jariwala, I.S. Kim, K.-S. Chen, T.J. Marks, L.J. Lauhon, and M.C. Hersam, *Gate-tunable memristive phenomena mediated by grain boundaries in single-layer $MoS_2$.* Nat Nanotechnol, 2015. **10**(5): p. 403-406.
49. Karban, P., F. Mach, P. Kůs, D. Pánek, and I. Doležel, *Numerical solution of coupled problems using code Agros2D.* Computing, 2013. **95**(1): p. 381-408.
50. Hatta, I., Y. Shiroishi, K.A. Müller, and W. Berlinger, *Critical behavior of the heat capacity in $SrTiO_3$.* Physical Review B, 1977.
51. Breckenfeld, E., R. Wilson, J. Karthik, A.R. Damodaran, D.G. Cahill, and L.W. Martin, *Effect of Growth Induced (Non)Stoichiometry on the Structure, Dielectric Response, and Thermal Conductivity of $SrTiO_3$ Thin Films.* Chemistry of Materials, 2012. **24**(2): p. 331-337.
52. Waser, R., T. Baiatu, and K.-H. Härdtl, *dc Electrical Degradation of Perovskite-Type Titanates: I, Ceramics.* Journal of the American Ceramic Society, 1990. **73**(6): p. 1645-1653.
53. Ngai, K.L. and A.K. Rizos, *Parameterless explanation of the non-arrhenius conductivity in glassy fast ionic conductors.* Phys Rev Lett, 1996. **76**(8): p. 1296-1299.
54. Eichel, R.-A., *Structural and dynamic properties of oxygen vacancies in perovskite oxides—analysis of defect chemistry by modern multi-frequency and pulsed EPR techniques.* Physical Chemistry Chemical Physics, 2011. **13**(2): p. 368-384.